Received: 30 March 2024 | Revised: 16 September 2024 | Accepted: 27 September 2024

IET Microwaves, Antennas & Propagation

DOI: 10.1049/mia2.12522

ORIGINAL RESEARCH

Classification with electromagnetic waves

Ergun Simsek | **Harish Reddy Manyam**

Department of Computer Science and Electrical Engineering, University of Maryland Baltimore County, Baltimore, Maryland, USA

Correspondence

Ergun Simsek.
Email: simsek@umbc.edu

Funding information

UMBC, Grant/Award Number: 7040330

Abstract

The integration of neural networks and machine learning techniques has ushered in a revolution in various fields, including electromagnetic inversion, geophysical exploration, and microwave imaging. While these techniques have significantly improved image reconstruction and the resolution of complex inverse scattering problems, this paper explores a different question: *Can near-field electromagnetic waves be harnessed for object classification?* To answer this question, we first create a dataset based on the MNIST dataset, where we transform the grayscale pixel values into relative electrical permittivity values to form scatterers and calculate the electromagnetic waves scattered from these objects using a 2D electromagnetic finite-difference frequency-domain solver. Then, we train various machine learning models with this dataset to classify the objects. When we compare the classification accuracy and efficiency of these models, we observe that the neural networks outperform others, achieving a 90% classification accuracy solely from the data without a need for projecting the input data into a latent space. The impacts of the training dataset size, the number of antennas, and the location of antennas on the accuracy and time spent during training are also investigated. These results demonstrate the potential for classifying objects with near-field electromagnetic waves in a simple setup and lay the groundwork for further research in this exciting direction.

KEYWORDS

electromagnetic wave scattering, learning (artificial intelligence), neural nets

1 | INTRODUCTION

In the fields of electromagnetic inversion, geophysical exploration, and microwave imaging, the primary objective is to extract valuable information about the internal structure of objects or scenes by analysing their interactions with electromagnetic waves [1–12]. Traditional methods in these areas often encounter challenges related to nonlinearity, ill-posedness, and high computational costs [1–12]. In recent years, many novel machine learning-based approaches have been proposed to address these issues in applications related to electromagnetics [13–25], geophysics [14, 26–30], and imaging [17, 31, 32]. For instance, in ref. [13], a cascade of multilayer complex-valued residual convolutional neural network (NN) modules is used to learn a general model for approximating the underlying electromagnetic inverse scattering system and then utilise this general model for solving highly nonlinear inverse scattering problems accurately. In another study [17], a novel NN architecture, termed the contrast source network, is introduced to address the issue of traditional techniques getting trapped in false local minima when recovering high permittivity objects. In ref. [23], the authors provide a very broad review of the recently developed deep learning-based approaches for solving electromagnetic inversion problems and recommend a learning-assisted objective-function approach to achieve accuracy with a desired level of confidence.

Abbreviations: BIM, Born Iterative Method; CSI, Contrast Source Inversion; DBIM, Distorted Born Iterative Method; GBG, Gaussian Naive Bayes; kNN, k-nearestneighbour; MNIST, Modified National Institute of Standards and Technology; NN, neural network; PCA, principal components analysis; RF, random forest; SVM, support vector machine; *t*-SNE, *t*-distributed stochastic neighbour embedding; XGB, gradient boosting.

The integration of neural networks and machine learning techniques has indeed significantly improved the quality and speed of image reconstruction, making it possible to tackle problems that were previously deemed impractical when using conventional methods. However, the central research question of this work, which differs from what has previously been considered, is, *Can we achieve the task of classification using electromagnetic data?* So instead of determining, for example, the electrical permittivity and conductivity distribution over a certain domain, we are primarily interested in determining the kinds (classes) of the objects that we have in that domain of interest.

In the field of computer vision, researchers— [33] and references therein—have developed computer systems that can automatically recognise and classify handwritten digits in images, finding applications in postal mail sorting, bank check processing, and form processing. The electromagnetic counterpart, which involves recognising and classifying objects using electromagnetic waves, has potential applications in robotics for enabling robots to perceive their environment and interact with objects. The use of electromagnetic waves for object recognition can offer advantages over conventional imaging systems, especially in scenarios where optical methods (e.g., cameras) are insufficient. For example, electromagnetic waves can penetrate certain materials that are opaque to visible light, enabling the detection of hidden or occluded objects. Furthermore, cameras rely on lighting conditions and may struggle to detect objects in low-visibility environments (such as fog, darkness, or smoke), whereas electromagnetic waves, particularly in specific frequency ranges like microwave or millimetre-wave, can provide more robust detection capabilities in these challenging environments.

In this work, we aim to determine whether it is possible to assign labels or categories to objects based on the electromagnetic waves scattered from these objects in a simple setup. We stress the emphasis on a simple setup, as some researchers have proposed sophisticated approaches to achieve classification using light in reservoir computing applications. For instance, in ref. [34], a new method for extreme deep learning using electromagnetic waves is proposed, utilising specially designed materials to create a nonlinear interaction between light waves of different frequencies. This interaction is then employed to perform complex learning tasks, such as forecasting chaotic time series or classifying various types of data. This describes a significant development in the field of wave-based computing and has the potential to lead to new types of optical computers that are much faster and more energy-efficient than traditional electronic computers. Nevertheless, the primary aim of our study is more straightforward: to classify individual objects based on electromagnetic data collected by antennas situated in close proximity to the objects scattering the waves. Successfully demonstrating this concept might open up the possibility of exploring the practical applications of electromagnetic wave-based classification in various real-world scenarios, particularly in the domains of robotics and object recognition. The key potential advantages of electromagnetic wave-based object classification over image-based recognition can be summarised as follows.

- One of the primary advantages of using electromagnetic waves, particularly at certain frequencies, is their ability to penetrate materials that are opaque to visible light. This means that our approach can detect and classify objects that are hidden behind obstructions, covered by certain materials, or located in environments where optical methods fail (e.g., smoke, fog, or darkness). Conventional image-based recognition systems, which rely on visible or near-visible light, would be severely limited or ineffective in such scenarios.
- Image-based pattern recognition systems rely on visual features (shape, colour, texture, etc.) to classify objects. However, they cannot directly discern the material properties of the objects they are identifying. In contrast, our method is sensitive to the dielectric properties of objects, which allows us to distinguish between materials that may appear visually similar but have different electromagnetic properties. This could be particularly useful in applications where material composition is a key factor, such as detecting hazardous materials, distinguishing between different types of plastics, or even identifying materials based on their electromagnetic response.
- Optical systems can be affected by environmental conditions such as lighting, shadows, or reflections, which can introduce noise or distortions in image recognition tasks. Electromagnetic wave-based systems, on the other hand, are less sensitive to such factors. They can operate effectively across various environments without the need for specific lighting conditions, making them more robust for real-world applications, especially in challenging or uncontrolled environments.
- Unlike conventional image recognition, which only captures surface information, electromagnetic wave scattering techniques have the potential for sub-surface imaging, allowing for classification of objects that are buried or embedded within other materials. This could be particularly useful in non-destructive testing, medical imaging, or geophysical exploration, where it is crucial to identify the objects beneath the surface.

It should also be noted that there are some other recent studies that have shown the integration of machine learning and electromagnetic wave analysis for material identification and classification. For example, Harrison et al., proposed a novel methodology for material identification using a microwave sensor array [35]. Unlike traditional systems that use a single resonating sensor, this method employs an array resonating at different frequencies to improve identification accuracy. Machine learning algorithms were applied to the collected data, and the approach was validated on various materials such as wood, cardboard, and plastics. In another work, Covarrubias-Martínez et al., introduced a method for classifying plastic materials using a microwave resonant sensor [36]. They evaluated several machine learning classifiers in material classification, accounting for uncertainties such as air gaps and pellet positions. Their approach presents a fast, non-destructive method for identifying plastic raw materials with

industrial potential. Both in refs. [35, 36], the resonances in the collected data play a crucial role because the primary intention is the material identification. In a very recent study, Ting et al., proposed a material classification system utilising an embedded random forest (RF) antenna array, which measures changes in the received signal strength indicator values [37]. The study combined a Kalman filter with a support vector machine (SVM) classifier, achieving over 96% accuracy in material classification within a 2-m range. Their system, designed for mobile robotic applications such as warehouse automation, focuses on real-time, proximal remote sensing of materials. Our work might be considered a numerical version of their experimental study.

The structure of this paper is as follows. First, we provide a brief overview of electromagnetic inversion and explain its main difference from electromagnetic classification. Then, we describe how we create our dataset. Note that the sample codes to produce the results presented in this work and the dataset can be found at ref. [38]. This dataset can be used for both electromagnetic classification and inversion problems. Third, we compare the classification accuracy and efficiency of several machine learning models trained to classify 10 labels from the electromagnetic data recorded by antennas placed around one-half of the domain of interest. Subsequently, we investigate how accuracy and training time change with the training dataset size, the number of antennas, and the location of antennas. Following some discussions, we present our conclusions.

2 | ELECTROMAGNETIC INVERSION VS. ELECTROMAGNETIC CLASSIFICATION

Consider a black box, as depicted in Figure 1a, surrounded by an array of transmitter and receiver antennas. Inside this black box, assume the presence of a concealed object characterised by relative electrical permittivity 3.5, as illustrated in Figure 1b. The surrounding medium is assumed to be air. In the context of this simplified electromagnetic inversion problem, wherein all materials involved are treated as lossless and non-magnetic dielectrics, the objective is to infer the permittivity distribution across the domain of interest based on the electromagnetic data acquired by the receiver antennas. One can solve this electromagnetic inversion problem numerically and iteratively [1–11, 23, 39] as follows.

Consider a scenario where there exist M_T illuminating sources for exciting the medium and M_R receivers for collecting the scattered field. Consequently, the overall number of acquired data points is denoted as $M = M_T \times M_R$. Let the reconstruction domain D be discretised into N small cells, with constant field quantities and contrast function within each cell. The total electric field at position $\mathbf{r}$ within the dielectric object, induced by an exciting source situated at $\mathbf{r}_T$, can be expressed as a sum of the incident and scattered fields. This summation is governed by the superposition principle and can be represented as follows:

$$\mathbf{E}(\mathbf{r},\mathbf{r}_T) = \mathbf{E}^{inc}(\mathbf{r},\mathbf{r}_T) + \left(k^2 + \nabla\nabla\cdot\right) \int_D \mathbf{G}^{AJ}(\mathbf{r},\mathbf{r}')\cdot\chi(\mathbf{r}')\mathbf{E}(\mathbf{r}',\mathbf{r}_T)d\mathbf{r}', \qquad \mathbf{r}\in D \tag{1}$$

where $\mathbf{G}^{AJ}(\mathbf{r},\mathbf{r}')$ is an auxiliary dyadic Green's function representing the magnetic vector potential, the wavenumber is given by $k^2 = \omega^2\mu\tilde{\epsilon}$ and $\chi(\mathbf{r})$ is the contrast, that is, $\chi(\mathbf{r}) = (\tilde{\epsilon}(\mathbf{r}) - \epsilon)/\tilde{\epsilon}$. Equation (1) is called the object equation, which is a Fredholm integral equation of the second kind for the unknown field inside the object. Once the total electric field is obtained, then the scattered field recorded at any of the receiver antennas, let's say located on path ℓ can be calculated with the data equation which defines the scattered field at the observation point, that is,

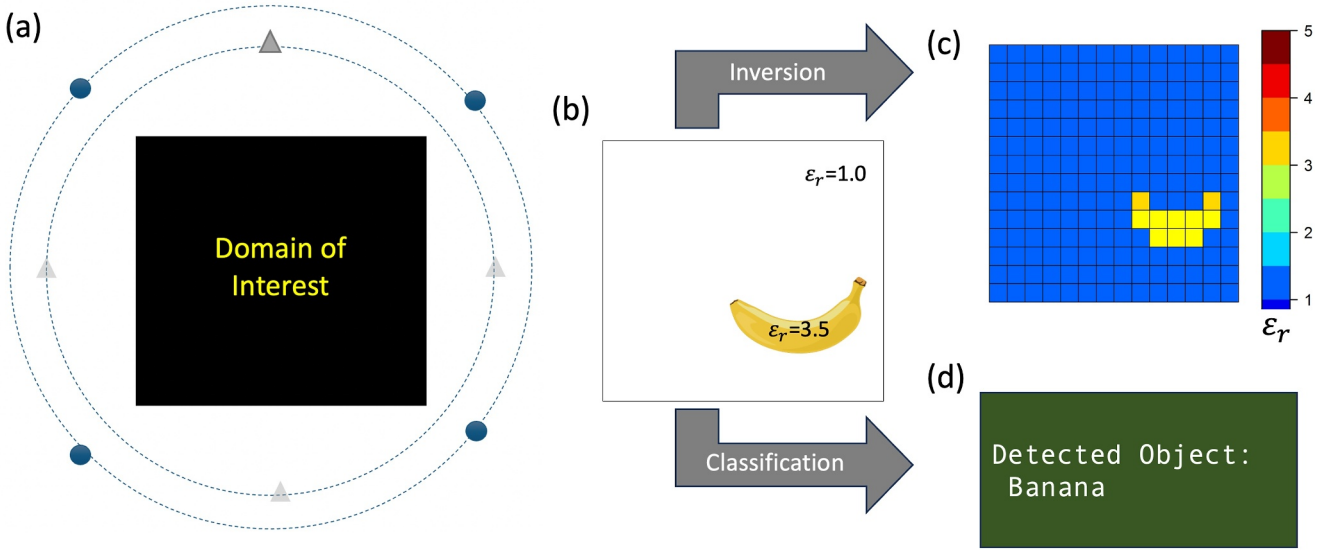

FIGURE 1 (a) Domain of interest is surrounded by a group of transmitter and receiver antennas, (b) an object embedded in the domain of interest, and a typical output of (c) an electromagnetic inversion and (d) electromagnetic classification.

$$\mathbf{E}_m^{sca}(\mathbf{r}, \mathbf{r}_T) = \mathrm{j}\omega\tilde{\epsilon} \int_D \mathbf{G}^{EJ}(\mathbf{r}, \mathbf{r}') \cdot \chi(\mathbf{r}')\mathbf{E}(\mathbf{r}', \mathbf{r}_T)d\mathbf{r}', \ \mathbf{r} \in \ell \quad (2)$$

where $\mathbf{G}^{EJ}(\mathbf{r}, \mathbf{r}')$ is the electric dyadic Green's function at the observation point $\mathbf{r}$ related to a unit current source at the point $\mathbf{r}'$.

The data equation, establishing the connection between the measured data and the unknown contrast of the material, can be expressed in a discretised form as follows:

$$\mathbf{f}(\mathbf{r}_{i_R}, \mathbf{r}_{i_T}) = \omega\tilde{\epsilon}_q \sum_{k=1}^{N} \mathbf{G}^{EJ}(\mathbf{r}_{i_R}, \mathbf{r}'_k) \cdot \mathbf{E}(\mathbf{r}'_k, \mathbf{r}_{i_T})\chi(\mathbf{r}'_k)\Delta S \quad (3)$$

where $\mathbf{f}$ is a $2M$-dimensional data column vector whose elements are given measured scattered electric field data, ΔS is the surface element, $i_R = 1, \ldots, M_R$ and $i_T = 1, \ldots, M_T$ denote indices for the receiver and transmitter, respectively. Note that if this was a three-dimensional problem, then $\mathbf{f}$ would be a $3M$-dimensional data and instead of surface element (ΔS), we would be using volume elements (ΔV). For M measurements and N discretised cells, Equation (3) can be written compactly as follows:

$$\mathbf{f} = \mathbf{M}\mathbf{x}, \quad (4)$$

where $\mathbf{x}$ is a N-dimensional column vector of the contrast function χ, and $\mathbf{M}$ is a $2M \times N$ matrix whose elements are given using the following equation:

$$\mathbf{M}_{ik} = \mathrm{j}\omega\tilde{\epsilon}_q \mathbf{G}^{EJ}_{mq}(\mathbf{r}_{i_R}, \mathbf{r}'_k) \cdot \mathbf{E}(\mathbf{r}'_k, \mathbf{r}_{i_T})\Delta S \quad (5)$$

where $i = i_R + (i_T - 1)M_R$, and $k = 1, \ldots, N$.

Since the total electric field $\mathbf{E}$ within the objects is an unknown function of the material contrast χ, Equation (4) becomes a nonlinear equation. Furthermore, the limited amount of available information renders the problem non-unique. This equation can be solved iteratively using either the Contrast Source Inversion (CSI) method [8, 9, 12], or the Born Iterative Method (BIM) [2, 7, 39], or the Distorted Born Iterative Method (DBIM) [10, 11, 39]. The CSI method constructs a sequence of contrast sources and contrasts iteratively without relying on a forward solver. While it is a stable method, it requires a large number of iterations to achieve the desired accuracy. Born Iterative Method and DBIM are commonly employed iterative methods for solving nonlinear inverse scattering problems, as they typically demand fewer iterations. The primary distinction between BIM and DBIM is that the latter utilises an updated background Green's function for each iteration, a necessity when addressing electromagnetic inversion problems involving inhomogeneous backgrounds, such as multi-layered media. Due to this difference, DBIM is computationally more expensive than BIM, but it boasts second-order convergence, whereas BIM only achieves first-order convergence. This computational cost/convergence order trade-off can be managed through a two-step algorithm, as elucidated in ref. [7].

Over the past two decades, both computational electromagnetics and geophysics societies have witnessed a growing interest in enhancing the efficiency of existing methodologies through the incorporation of machine learning techniques, with a particular emphasis on the application of deep learning. This convergence marks a significant paradigm shift in the pursuit of optimising electromagnetic and geophysical simulations for diverse applications. One major avenue of exploration involves training neural networks to directly reconstruct the contrast of scatterers based on the measured scattered fields [13–16, 28, 40, 41]. This approach capitalises on the inherent capacity of deep learning models to discern complex patterns and relationships within datasets. By leveraging these capabilities, researchers aim to enhance the accuracy and speed of contrast reconstruction, enabling a more precise representation of the underlying electromagnetic or geophysical properties. In parallel, another compelling avenue unfolds where neural networks are harnessed to learn dynamically throughout the iterative solution process [17, 18, 20–22, 24, 25, 30, 31]. This innovative approach stands in contrast to traditional methods by enabling the network to adapt and refine its understanding of the problem space as the solution evolves. Through this adaptive learning process, neural networks can capture intricate features and nuances in the data, thereby contributing to more robust and efficient solutions.

However, the focus here is not on determining the permittivity distribution across the domain of interest. Instead, the objective is to identify the object within the black box, exemplified in Figure 1d. One possible approach to tackle this classification task involves training neural networks, with the input data being the electromagnetic data recorded by the receiver antennas and the outputs corresponding to the object types (classes). Given the absence of an extensive dataset conducive to such a study, the subsequent section outlines our efforts to generate one from a well-established dataset, as detailed below.

3 | THE DATASET

The Modified National Institute of Standards and Technology (MNIST) dataset [42] is a collection of handwritten digits and widely used in the field of machine learning and computer vision for training and testing various machine learning algorithms, particularly for tasks like image classification and character recognition. It consists of 28×28-pixel square grayscale images of handwritten digits, ranging from 0 to 9. Each image is associated with a corresponding label that specifies which digit the handwritten image represents.

In this work, the 60,000 digital images of the MNIST dataset are used to create a scatterer database as follows. In the MNIST dataset, the value of each pixel in an image represents the grayscale intensity of that pixel. The pixel values, $d_{u,v}$ for $u, v = 1, 2, \ldots, 28$, are typically scaled to fall within a range of 0–255, with 0 indicating white (no ink) and 255 indicating black (maximum ink saturation). Values between 0 and 255 represent

various shades of grey. These values can be converted into relative electrical permittivity values ranging from $\epsilon_r^{\min}$ to $\epsilon_r^{\max}$ using the following equation:

$$\epsilon_r(u,v) = \epsilon_r^{\min} + \left(\epsilon_r^{\max} - \epsilon_r^{\min}\right)\frac{d_{u,v}}{255} \tag{6}$$

where u and v are the row and column numbers. We set $\epsilon_r^{\min} = 1$ and $\epsilon_r^{\max} = 4$ for the reasons that are discussed below.

To create the electromagnetic scattering dataset, we utilise a freely available 2D electromagnetic finite difference frequency domain simulation tool called Ceviche [43]. The computation domain, shown in Figure 2a, has dimensions of $2\lambda \times 2\lambda$ and is uniformly meshed along the x and y directions, with $\Delta x = \Delta y = \lambda/150$, where λ represents the wavelength of the electromagnetic waves generated by a transmitter antenna with a length of λ. The thickness of the perfectly matched layers along all directions is $\lambda/7.5$. Initially, the permittivity of each cell is assumed to be 1.

Since the original files in the MNIST dataset (28×28 pixels) are too small compared to our computation domain (300×300 pixels), we use a 2D cubic interpolation to update the permittivity of the 140-pixel by 140-pixel region at the centre of the computation domain with the permittivity values obtained using Equation (6), as illustrated in Figure 2a. Figure 2b displays the permittivity distribution across the computation domain for one of the examples studied in this work. In this setup, we consider two groups of receiver antennas. The first group comprises $N_r/2$ receiver antennas uniformly placed between $x = 0.4\lambda$ and $x = 1.57\lambda$ at $y = 1.6\lambda$, while the second group consists of $N_r/2$ receiver antennas uniformly placed between $y = 0.4\lambda$ and $y = 1.57\lambda$ at $x = 1.6\lambda$, where N_r is an even integer that represents the total number of receiver antennas. Note that these antennas are not intended to physically capture the permittivity values of each pixel but rather capture the scattered electromagnetic fields resulting from the permittivity distributions created with Equation (6) from the pixelated MNIST images. The connection lies in how the pixel values of the MNIST images affect the permittivity distribution, which in turn influences the electromagnetic fields that the antennas record. Additionally, there are two transmitter antennas: transmitter antenna-1 is positioned at $x = 0.2\lambda$ between $y = 0.5\lambda$ and $y = 1.5\lambda$, while transmitter antenna-2 is situated at $y = 0.2\lambda$ between $x = 0.5\lambda$ and $x = 1.5\lambda$. Since we treat the problem as a 2D problem, we only deal with three field components: the z component of the electric field (E_z) and the x and y components of the magnetic field (H_x and H_y). We begin by assuming that transmitter antenna-1 is active and proceed to calculate E_z, H_x, and H_y at N_r receiver antennas. We then repeat this process, assuming that only transmitter antenna-2 is active. The real and imaginary parts of the calculated electric and magnetic fields are stored in separate columns of the dataset. Consequently, the input section of the dataset consists of 60,000 rows and 624 columns. These 624 columns represent the maximum number of receiver antennas, $N_r^{\max} = 52$, two transmitter antennas, three fields, and two components (real and imaginary parts). The output section of the dataset consists of the labels (digits), resulting in a $60,000 \times 1$ vector. Note that in the first part of the numerical studies, we only 10 receiver antennas. The reason we record the electric field intensities at 52 different locations is that in the second part of the numerical studies, we aim to

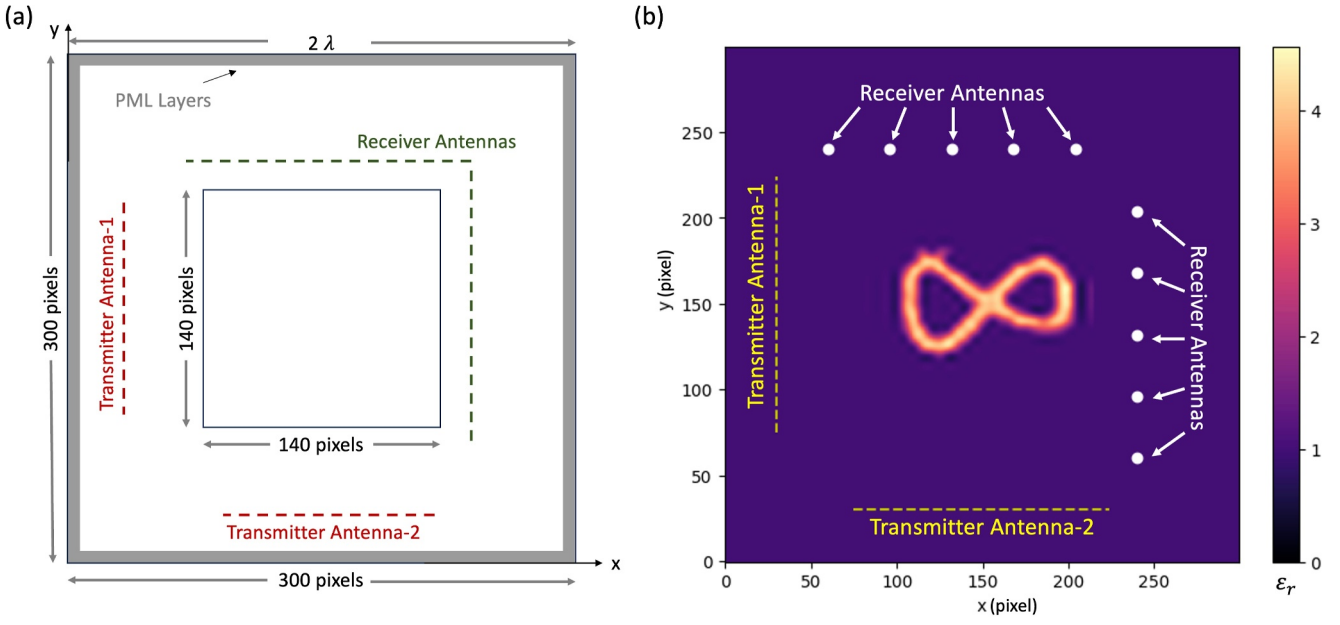

FIGURE 2 (a) The computation domain covers a 2λ by 2λ region that is uniformly meshed along the x and y axes at a mesh sampling density of $\lambda/150$. Grey-shaded areas represent the perfectly matched layers. (b) Permittivity distribution for one of the example geometries studied. The purple regions have a relative permittivity of 1. The regions with higher relative permittivity values are represented by lighter colours. The locations of transmitter antennas are indicated by yellow dashed lines, while white circles depict the positions of the 52 receiver antennas.

determine the affect of antenna locations and inter-antenna spacing on the classification accuracy.

For the sake of brevity, we do not provide a figure that depicts the electric field intensities ($|E_z|$) recorded by the receiver antennas for each label, but we would like to briefly emphasise that there is no clear pattern recognisable by humans for identifying the labels from the field profiles. Also, to investigate the complexity of our data, we project 5000 samples from our dataset to two latent spaces using principal components analysis (PCA) [44, 45] and *t*-distributed stochastic neighbour embedding (*t*-SNE) [45, 46]. The visualisations are provided in Figure 3. Unlike for the original MNIST dataset [45], here we do not have a clear interpretation even after projections.

4 | MACHINE LEARNING MODELS

We employ various machine-learning models, namely k-nearest neighbour (kNN), RF, Gaussian Naive Bayes (GNB), SVM, gradient boosting (XGB), and a NN, to assess whether they exhibit similar levels of learning from the data or not. For the first four models (kNN, RF, GNB, and SVM), we utilise scikit-learn [47], which is a free software machine learning library for the Python programming language. For the XGB implementation, we use another freely available library [48], which is developed based on XGBoost [49]. Hyperparameter tuning is done using the Grid Search Cross-Validation (GridSearchCV) module [50] that is available in the scikit-learn [47] library.

For the NN implementations, we employ Keras' [51] functional application programme interface running on top of TensorFlow [52]. The model starts with an input layer of N_c dimensions, where $N_c = 12 \times N_r$ is the number of columns of our input data, followed by a dense layer with 500 units, utilising the *HeNormal* weight initialisation [53] and employing the rectified linear unit activation function [54]. Subsequently, another dense layer with 250 units continues the flow, maintaining the same initialisation and activation choices. To enhance the model's robustness, a dropout layer with a dropout rate of 0.2 is introduced to mitigate overfitting. The architecture then proceeds with a dense layer of 100 units, followed by a smaller layer with 30 units, both sharing the same initialisation and activation configurations. To further optimise the network, a batch normalisation layer is integrated, contributing to the stability and efficiency of the learning process. The final touch is a dense layer with 10 units and a softmax activation function [55], tailored for a classification task with 10 output classes. The model's learning process is guided by the Adam optimiser [56], with a learning rate set at 0.001. The categorical cross-entropy loss [57] is chosen as the optimisation objective, and categorical accuracy is monitored as a metric to gauge performance. During training, adaptive strategies are implemented. Specifically, a learning rate reduction is triggered by the *ReduceLROnPlateau* callback, which responds to changes in validation categorical accuracy. Additionally, the *EarlyStopping* callback monitors the same metric, terminating training early if improvements plateau for an extended period. To ensure the preservation of the best-performing model, the *ModelCheckpoint* callback is employed. It saves the model whenever a new high in validation categorical accuracy is achieved, promoting the retention of optimal weights. The architecture as a whole embodies a holistic approach, combining architectural choices and training strategies for an effective and adaptive NN. All the code is executed on Google Colaboratory using T4 GPU accelerators.

5 | NUMERICAL RESULTS

In this section, we first evaluate the accuracy of two machine learning models and then investigate how different factors, such as dataset size and the number and location of antennas, influence the results.

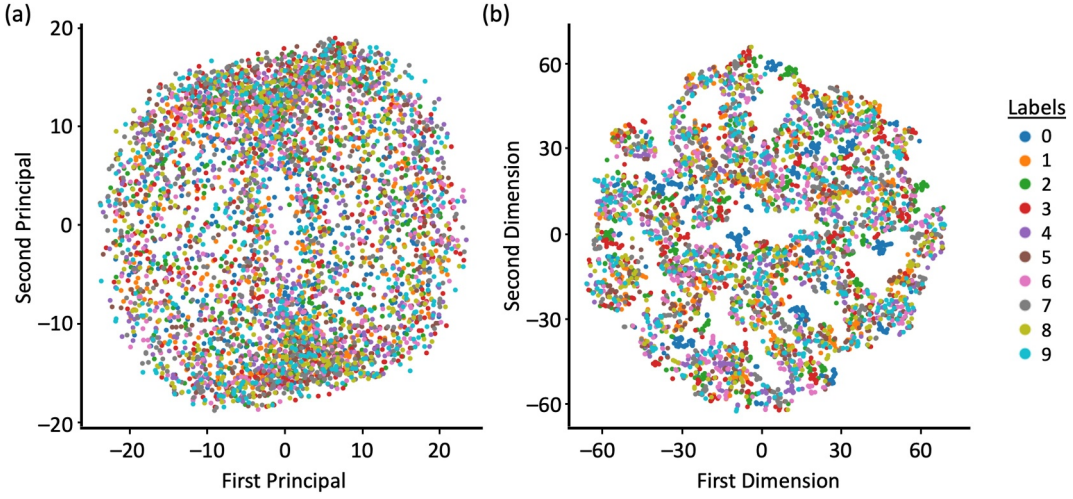

FIGURE 3 Visualisations of the labels in two latent spaces obtained with (a) principal components analysis (PCA) and (b) *t*-SNE.

5.1 | Accuracy of different ML methods

For the initial set of calculations, we use 10 receiver antennas and allocate 50% of the dataset for training and the other 50% for testing. Table 1 presents the time spent during training for each model, as well as their accuracy, precision, recall, and F1 scores. We observe that SVM, XGB, and NN implementations achieve higher accuracy (>80%), precision, recall, and F1 scores compared to the kNN, RF, and GNB implementations. Although the NN's training time is longer than the SVM and XGB, it delivers the highest classification accuracy (90.17%). This result is promising but not surprising, given the NN's ability to identify extremely complex patterns when trained on sufficiently large datasets. It is worth noting that the classification accuracy obtained with the NN is higher than the previously reported value [34] of 85.3%.

TABLE 1 The time spent during training, accuracy, precision, recall, and F1-score of the k-nearest neighbour (kNN), random forest (RF), Gaussian Naive Bayes (GNB), support vector machine (SVM), gradient boosting (XGB), and neural network (NN) implementations using the 50% of the dataset for training and the remaining 50% for testing.

Method	Time (s)	Accuracy	Precision	Recall	F1 score
kNN	0.1	0.66	0.67	0.66	0.65
RF	495	0.76	0.75	0.75	0.75
GNB	0.52	0.61	0.61	0.60	0.60
SVM	296	0.85	0.85	0.85	0.85
XGB	183.7	0.84	0.84	0.84	0.84
NN	434	0.90	0.90	0.90	0.90

Figure 4 displays the confusion matrix of the NN implementation, revealing that the most accurately classified label is 1, while eight is the least accurately classified. Notably, 5.7% and 3.8% of objects labelled as 8 are in fact 3 and 5s.

One of the significant advantages of working with neural networks is the ease with which you can quantify and visualise the learning process's efficiency. Figure 5a,b illustrate how accuracy and loss change with respect to the epoch number for both training (solid curves) and validation (dashed curves). The little misalignment of these curves informs us that the number of neurons in the NN architecture is slightly higher than the optimal but the overfitting is not serious. The convergent behaviour observed in both figures indicates that the number of epochs used during the training is sufficient. In the same figure, we also observe that the training is ended at the 68th

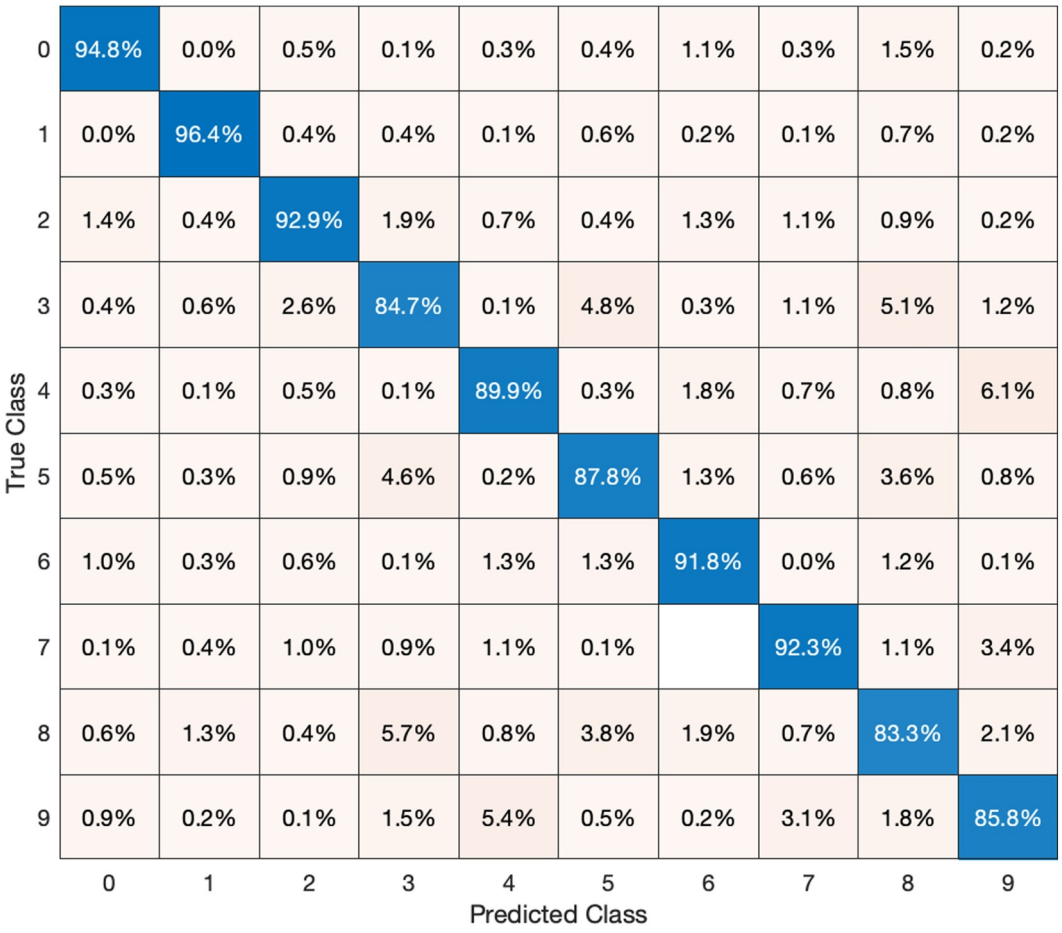

FIGURE 4 Confusion matrix of the neural network (NN) implementation. Since none of the 7s is predicted as a 6, the corresponding cell is blank.

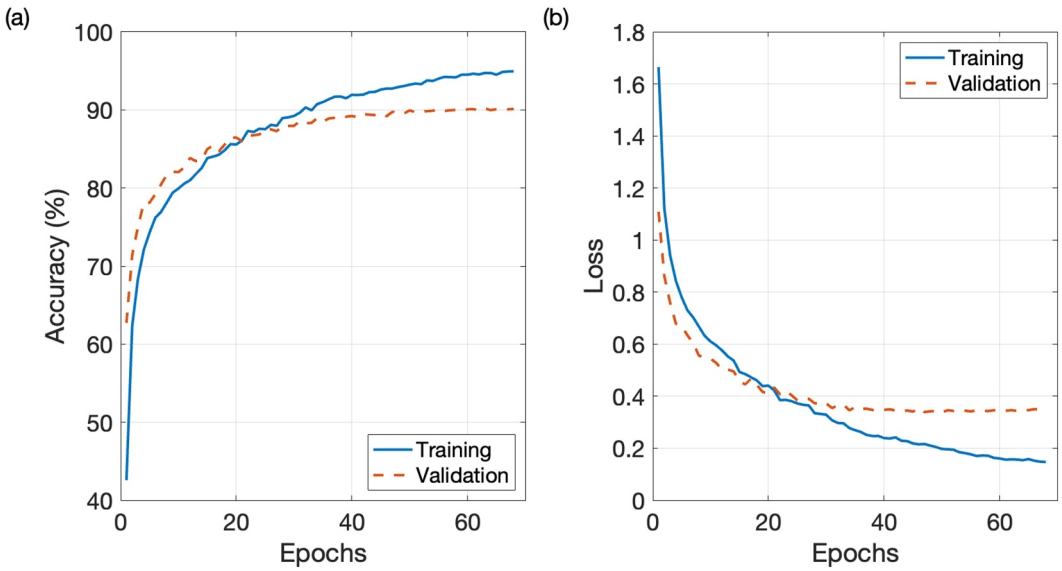

FIGURE 5 (a) Accuracy and (b) loss versus epoch number of the neural network (NN) implementation, which uses 50% of the dataset for training and the remaining 50% for testing.

epoch even the number of epochs is set to 100 thanks to the *EarlyStopping* callback monitor. Also, the learning rate is dropped from 10^{-3} to 4.398×10^{-5} in 14 steps triggered by the *ReduceLROnPlateau* callback.

Machine learning-based computer vision algorithms can achieve a classification accuracy of over 97% for handwritten digits [33]. However, these studies typically use all pixels to achieve such high accuracy, while we use only electromagnetic data recorded by antennas placed on two one-dimensional lines near the objects. Therefore, we consider a 90% classification accuracy using electromagnetic waves to be a successful approach.

5.2 | Influence of dataset size and number and location of antennas on the accuracy

For the results presented in Table 1 and Figures 4 and 5, we use 50% of the data for training, with the remaining 50% used for testing. In other words, we use 30,000 samples for training and other 30,000 samples that have not been seen by the NN before for testing. To examine the impact of the training dataset size (N_{train}) on accuracy and training time, we conduct an additional two sets of calculations. For the first set, we use 10% of the data for training ($N_{\text{train}} = 6000$) and the remaining 90% for testing. For the second set, we use 1% of the data for training ($N_{\text{train}} = 600$) and the remaining 99% for testing. The accuracy of each method is listed in Table 2. As expected, the accuracies drop for all methods. However, we would like to emphasise one important detail: NN is the most accurate when the dataset is large enough (N_{train} is 6000 or higher in this case), however, their accuracy drops significantly for small datasets and other methods–such as XGB in this case–can perform better. We might conclude that if we are going to implement a NN for object classification, then we should have a large enough dataset to achieve high accuracy.

TABLE 2 Accuracy (in percentile) of the k-nearest neighbour (kNN), random forest (RF), Gaussian Naive Bayes (GNB), support vector machine (SVM), XGB, and neural network (NN) implementations using 50%, 10%, and 1% of the dataset for training and the remaining data for testing.

Training/Testing ratio	kNN	RF	GNB	SVM	XGB	NN
50%/50%	66	76	61	85	84	90
10%/90%	56	67	55.5	76	79	81
1%/99%	29	48	37	49	57	54

Next, we investigate the influence of the number of antennas over the accuracy as follows. For the three cases above, where the training dataset size is changed from 50% to 10% first and then to 1%, we decrease the number of receiver antennas from 10 to 8, 4, and 2, and monitor the accuracy and training times. The results are plotted in Figure 6. Note that the number of transmitter antennas is still 2, which means that the number of data points is $2 \times N_r$. As we examine Figure 6a–c, we first observe that both the accuracy and training times decrease with decreasing dataset size but the accuracy remains almost constant when the receiver antenna number is reduced from 10 to 4. Hence, we might claim that having an inter-antenna spacing of $\lambda/4$ is adequate for accurate classification as long as we have a large training dataset. In terms of training time, we observe a slight decrease in training times with a decreasing number of antennas, but this decrease is not linear and the main factor that determines the training time is the dataset size.

Next, we investigate the influence of antenna locations over the accuracy as follows. Since the accuracy significantly drops when we have two receiver antennas only, we first start

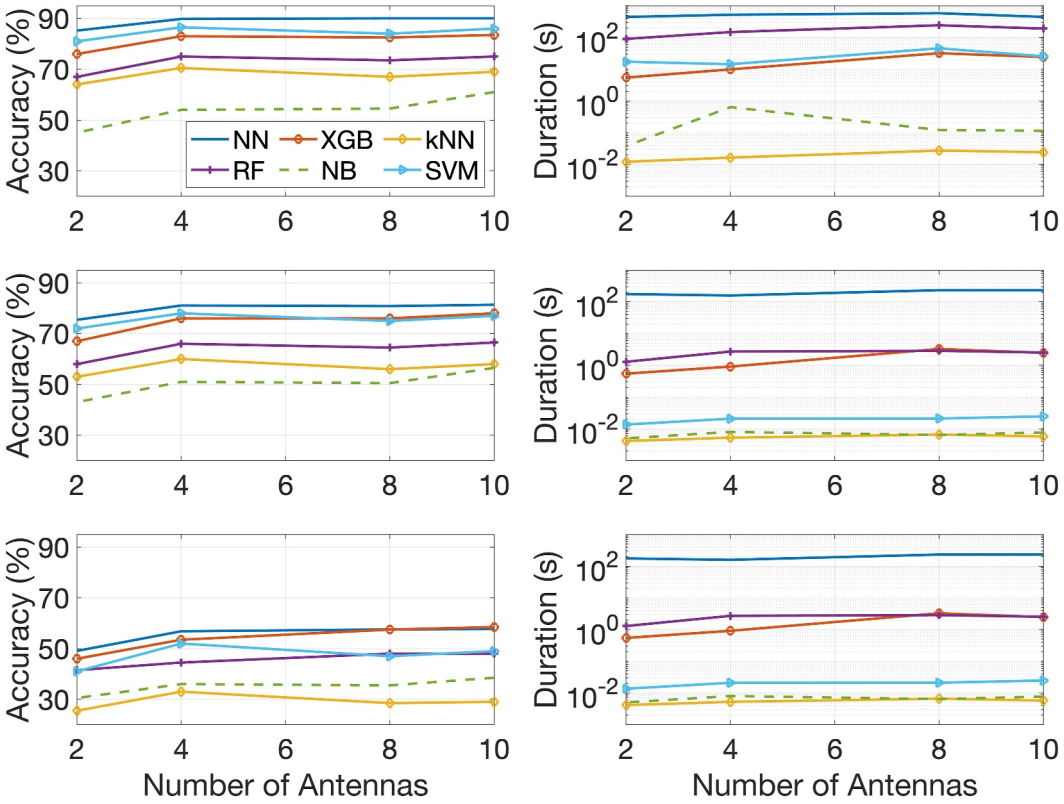

FIGURE 6 (left) Accuracy and (right) training time as a function of the number of receiver antennas when (a) $N_{\text{training}} = 15000$, (b) $N_{\text{training}} = 6000$, and (c) $N_{\text{training}} = 600$.

investigating this scenario by creating pairs of antennas by selecting one antenna from the top antenna group and one antenna from the side antenna group at a time. As mentioned before, our dataset includes field intensities recorded at 52 different locations. Here, for the pair-i, we select antennas R_i and R_{i+26} for $i = 1, 2, \ldots, 13$ as shown in Figure 7a for the first two pairs, and we monitor the accuracy. The blue curve in Figure 7c shows how the accuracy changes with the pair number. Even though the results change slightly ($\pm 0.6\%$), we can understand the trend (peaking near the middle), by considering the following two facts: (i) the scatterers are placed parallel to the x-axis, so the antennas from the top group are likely to carry more information about the scatterer than the side antennas, and (ii) when we increase i, we get closer to the scatterer centre but at the same time, the distance between the left transmitter antenna and i^{th} receiver antenna increases while the distance between the bottom transmitter antenna and $i + 26^{th}$ receiver antenna decreases.

Then we repeat the same procedure for groups of 4 antennas at a time. In this case, the group-i is formed by select antennas R_i and R_{i+13} from the top group and antennas R_{i+26} and R_{i+39} from the side group as shown in Figure 7b for the first two groups. How accuracy changes with the group number is depicted with the red curve in Figure 7c. In this case, the accuracy decreases almost steadily. Again, we believe that the increasing distance from the left transmitter antenna with increasing i and hence the weakening scattering data is the main cause of this decaying accuracy.

6 | DISCUSSIONS

In this work, the main aim was to achieve high classification accuracy without projecting the input data into a latent space. If such projections, for example, PCA, are used, both neural networks and gradient-boosted decision trees achieve the same accuracy. However, it should be noted that unlike the original MNIST dataset, here we have to utilise more than 30 principal components to achieve a 90% accuracy due to the complex nature of electromagnetic scattering data. If 20 principal components or fewer are used, the accuracy drops significantly. Figure 8 shows the explained variance ratio of the first 40 principal components on a logarithmic scale.

The accuracy of the classification depends on the permittivity range of the scatterers. In this work, we choose the maximum allowed relative permittivity to be 4 for two reasons. First, such narrow permittivity ranges, where $\epsilon_r^{\max}/\epsilon_r^{\min} < 10$ are already being reported, for example, in [58]. Second, larger permittivity values would impede the propagation of electromagnetic waves through the objects. For instance, if the maximum allowed electrical permittivity is set to 12, the accuracy of the NN implementation drops to 79%, primarily due

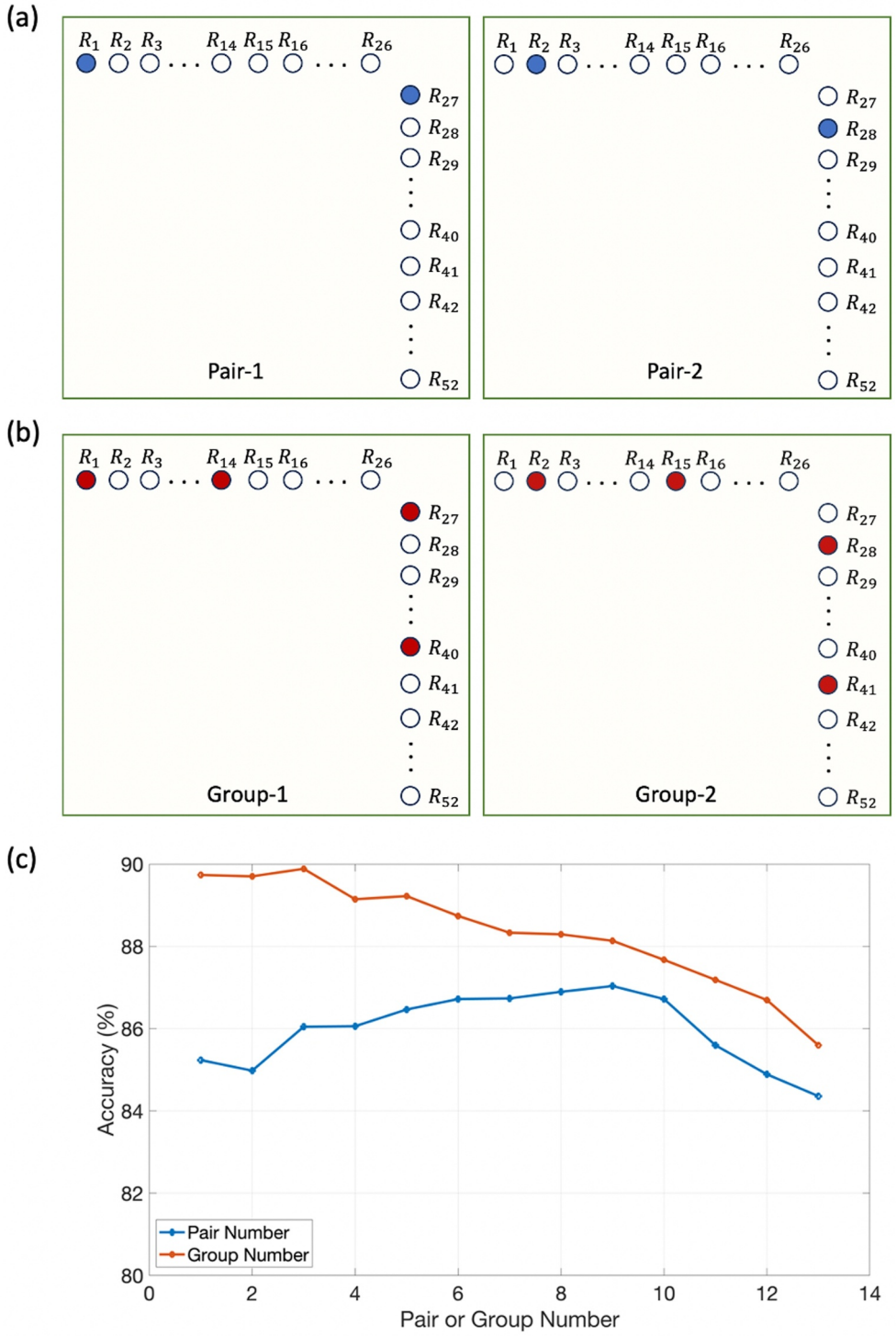

FIGURE 7 (a) Pairing two antennas by selecting only one antenna from the top antenna group and one antenna from the side antenna group, (b) grouping 4 antennas by selecting two antennas from the top and side antenna groups while keeping the inter-antenna distance fixed, (c) accuracy versus pair or group number.

to the strong reflectance from the objects back to the transmitter antennas.

Another important factor is the orientation of the scatterers. In this study, all the scatterers were parallel to the x-axis. When we rotate the scatterers, we observe that the accuracy of classification decreases to 58%. To achieve higher accuracy for objects with arbitrary alignments, it is necessary to place receiver antennas all around the domain of interest.

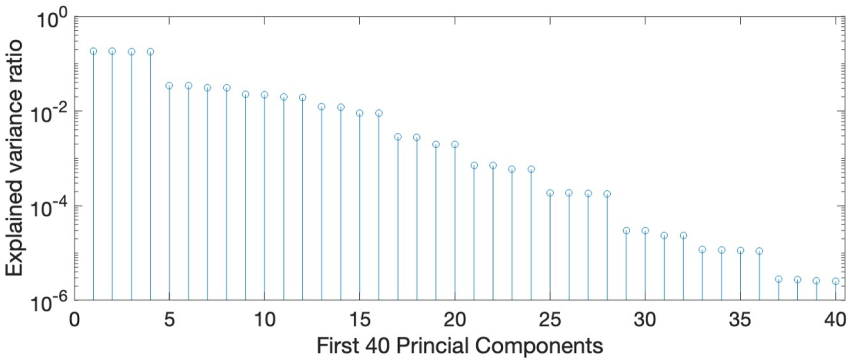

FIGURE 8 Explained variance ratio of the first 40 principal components in a logarithmic scale.

7 | CONCLUSION

In this paper, we have explored the application of machine learning and NN techniques in the context of electromagnetic wave-based object classification. The objective of our work was to determine whether it is feasible to classify objects based on the electromagnetic waves scattered from them in a simple experimental setup. We began by creating a dataset using the MNIST data, where we transformed grayscale pixel values into relative electrical permittivity values. A 2D electromagnetic finite difference frequency domain simulation tool was employed to calculate the electric and magnetic field data recorded by receiver antennas placed around the objects partially. We evaluated the classification performance of various machine learning models, including kNN, RF, GNB, SVM, gradient boosting, and a NN. The NN architecture demonstrated the highest accuracy, achieving an 90% classification accuracy. We also investigated the impact of the training dataset size, number of antennas, and location of antennas on accuracy and training time, highlighting the advantages of using a NN, especially as the dataset size is increased. However, we also observe that the number of samples of the dataset is more important than the number of receiver antennas to achieve a high accuracy to classify objects whose dimensions are close to the wavelength of excitation and we use four or more receiver antennas placed uniformly over one wavelength long region. While computer vision algorithms can achieve higher accuracy for handwritten digit recognition, our approach demonstrates that classifying objects using electromagnetic waves is a promising avenue. This research opens the door to exploring the potential of electromagnetic wave-based classification for various applications, including robotics and object recognition.

AUTHOR CONTRIBUTIONS

Ergun Simsek: Conceptualisation; Data curation; Formal analysis; Investigation; Methodology; Project administration; Supervision; Validation; Visualisation; Writing - original draft; Writing - review & editing. **Harish Reddy Manyam**: Investigation; Validation.

CONFLICT OF INTEREST STATEMENT

The authors declare no conflicts of interest.

DATA AVAILABILITY STATEMENT

Sample codes to produce the results presented in this work and the dataset can be found at https://github.com/simsekergun/CwEMW. This dataset can be used for both electromagnetic classification and inversion problems.

ORCID

Ergun Simsek https://orcid.org/0000-0001-9075-7071

REFERENCES

1. Bucci, O.M., Isernia, T.: Electromagnetic inverse scattering: retrievable information and measurement strategies. Radio Sci. 32(6), 2123–2137 (1997). https://doi.org/10.1029/97rs01826
2. Wang, Y.M., Chew, W.C.: An iterative solution of the two-dimensional electromagnetic inverse scattering problem. Int. J. Imag. Syst. Technol. 1(1), 100–108 (1989). https://doi.org/10.1002/ima.1850010111
3. Chen, X.: Computational Methods for Electromagnetic Inverse Scattering, vol. 244. Wiley Online Library (2018). https://doi.org/10.1002/9781119311997
4. Egbert, G.D., Kelbert, A.: Computational recipes for electromagnetic inverse problems. Geophys. J. Int. 189(1), 251–267 (2012). https://doi.org/10.1111/j.1365-246x.2011.05347.x
5. Abubakar, A., et al.: Inversion algorithms for large-scale geophysical electromagnetic measurements. Inverse Probl. 25(12), 123012 (2009). https://doi.org/10.1088/0266-5611/25/12/123012
6. Dorn, O., et al.: A nonlinear inversion method for 3D electromagnetic imaging using adjoint fields. Inverse Probl. 15(6), 1523–1558 (1999). https://doi.org/10.1088/0266-5611/15/6/309
7. Wei, B., et al.: Three-dimensional electromagnetic nonlinear inversion in layered media by a hybrid diagonal tensor approximation: stabilized biconjugate gradient fast Fourier transform method. Waves Random Complex Media 17(2), 129–147 (2007). https://doi.org/10.1080/17455030601016117
8. Abubakar, A., van den Berg, P.M.: Three-dimensional nonlinear inversion in cross-well electrode logging. Radio Sci. 33(4), 989–1004 (1998). https://doi.org/10.1029/98rs00975
9. Abubakar, A., Van den Berg, P., Semenov, S.Y.: Two-and three-dimensional algorithms for microwave imaging and inverse scattering. J. Electromagn. Waves Appl. 17(2), 209–231 (2003). https://doi.org/10.1163/156939303322235798
10. Cui, T.J., Chew, W.C.: Novel diffraction tomographic algorithm for imaging two-dimensional targets buried under a lossy earth. IEEE Trans. Geosci. Rem. Sens. 38(4), 2033–2041 (2000). https://doi.org/10.1109/36.851784
11. Cui, T.J., et al.: Inverse scattering of two-dimensional dielectric objects buried in a lossy earth using the distorted Born iterative method. IEEE Trans. Geosci. Rem. Sens. 39(2), 339–346 (2001). https://doi.org/10.1109/36.905242

12. Yu, C., Song, L.P., Liu, Q.H.: Inversion of multi-frequency experimental data for imaging complex objects by a DTA–CSI method. Inverse Probl. 21(6), S165–S178 (2005). https://doi.org/10.1088/0266-5611/21/6/s12
13. Li, L., et al.: DeepNIS: deep neural network for nonlinear electromagnetic inverse scattering. IEEE Trans. Antennas Propag. 67(3), 1819–1825 (2019). https://doi.org/10.1109/tap.2018.2885437
14. Yao, H.M., Jiang, L., Sha, W.E.I.: Enhanced deep learning approach based on the deep convolutional encoder–decoder architecture for electromagnetic inverse scattering problems. IEEE Antennas Wireless Propag. Lett. 19(7), 1211–1215 (2020). https://doi.org/10.1109/lawp.2020.2995455
15. Xu, K., et al.: Deep learning-based inversion methods for solving inverse scattering problems with phaseless data. IEEE Trans. Antennas Propag. 68(11), 7457–7470 (2020). https://doi.org/10.1109/tap.2020.2998171
16. Simsek, E.: Machine learning exercises on 1-D electromagnetic inversion. IEEE Trans. Antennas Propag. 69(10), 6797–6805 (2021). https://doi.org/10.1109/tap.2021.3069519
17. Sanghvi, Y., Kalepu, Y., Khankhoje, U.K.: Embedding deep learning in inverse scattering problems. IEEE Trans. Comput. Imaging 6, 46–56 (2020). https://doi.org/10.1109/tci.2019.2915580
18. Xiao, L.Y., et al.: Dual-module NMM-IEM machine learning for fast electromagnetic inversion of inhomogeneous scatterers with high contrasts and large electrical dimensions. IEEE Trans. Antennas Propag. 68(8), 6245–6255 (2020). https://doi.org/10.1109/tap.2020.2990222
19. Guo, R., et al.: Physics embedded deep neural network for solving full-wave inverse scattering problems. IEEE Trans. Antennas Propag. 70(8), 6148–6159 (2022). https://doi.org/10.1109/tap.2021.3102135
20. Fei, J., et al.: Fast 3-D electromagnetic full-wave inversion of dielectric anisotropic objects based on ResU-Net enhanced by variational born iterative method. IEEE Trans. Antenn. Propag. 70(8), 6229–6239 (2022). https://doi.org/10.1109/tap.2021.3138551
21. Shan, T., et al.: Neural Born iterative method for solving inverse scattering problems: 2D cases. IEEE Trans. Antennas Propag. 71(1), 818–829 (2023). https://doi.org/10.1109/tap.2022.3217333
22. Khorashadizadeh, A., et al.: Deep injective prior for inverse scattering. IEEE Trans. Antennas Propag. 71(11), 8894–8906 (2023). https://doi.org/10.1109/tap.2023.3312818
23. Chen, X., et al.: A review of deep learning approaches for inverse scattering problems (invited review). Prog. Electromagn. Res. 167, 67–81 (2020). https://doi.org/10.2528/pier20030705
24. Adler, J., Öktem, O.: Solving ill-posed inverse problems using iterative deep neural networks. Inverse Probl. 33(12), 124007 (2017). https://doi.org/10.1088/1361-6420/aa9581
25. Chen, G., et al.: Learning-assisted multimodality dielectric imaging. IEEE Trans. Antennas Propag. 68(3), 2356–2369 (2019). https://doi.org/10.1109/tap.2019.2948565
26. Giannakis, I., Giannopoulos, A., Warren, C.: A machine learning-based fast-forward solver for ground penetrating radar with application to full-waveform inversion. IEEE Trans. Geosci. Rem. Sens. 57(7), 4417–4426 (2019). https://doi.org/10.1109/tgrs.2019.2891206
27. Hu, Y., et al.: A supervised descent learning technique for solving directional electromagnetic logging-while-drilling inverse problems. IEEE Trans. Geosci. Rem. Sens. 58(11), 8013–8025 (2020). https://doi.org/10.1109/tgrs.2020.2986000
28. Liu, B., et al.: Deep learning inversion of electrical resistivity data. IEEE Trans. Geosci. Rem. Sens. 58(8), 5715–5728 (2020). https://doi.org/10.1109/tgrs.2020.2969040
29. Simsek, E.: Determining optical constants of 2D materials with neural networks from multi-angle reflectometry data. Mach. Learn.: Sci. Technol. 1(1), 01LT01 (2020). https://doi.org/10.1088/2632-2153/ab6d5f
30. Chen, X.: Subspace-based optimization method for solving inverse-scattering problems. IEEE Trans. Geosci. Rem. Sens. 48(1), 42–49 (2009). https://dx.doi.org/10.1109/TGRS.2009.2025122
31. Shao, W., Du, Y.: Microwave imaging by deep learning network: feasibility and training method. IEEE Trans. Antennas Propag. 68(7), 5626–5635 (2020). https://doi.org/10.1109/tap.2020.2978952
32. Suzuki, K.: Overview of deep learning in medical imaging. Radiol. Phys. Technol. 10(3), 257–273 (2017). https://doi.org/10.1007/s12194-017-0406-5
33. Andina, D., et al.: Deep learning for computer vision: a brief review. Comput. Intell. Neurosci. 2018, 1–13 (2018). https://doi.org/10.1155/2018/7068349
34. Momeni, A., Fleury, R.: Electromagnetic wave-based extreme deep learning with nonlinear time-Floquet entanglement. Nat. Commun. 13(1), 2651 (2022). https://doi.org/10.1038/s41467-022-30297-5
35. Harrison, L., et al.: Material identification using a microwave sensor array and machine learning. Electronics 9(2), 288 (2020). https://doi.org/10.3390/electronics9020288
36. Covarrubias-Martínez, D., et al.: Classification of plastic materials using machine-learning algorithms and microwave resonant sensor. J. Electromagn. Waves Appl. 36(12), 1760–1775 (2022). https://doi.org/10.1080/09205071.2022.2043192
37. Ting, T.M., Ahmad, N.S., Goh, P.: Material classification via embedded RF antenna array and machine learning for intelligent mobile robots. Alex. Eng. J. 106, 60–70 (2024). https://doi.org/10.1016/j.aej.2024.06.083
38. Simsek, E.: Classification with electromagnetic waves. GitHub (2023). https://github.com/simsekergun/CwEMW
39. Li, F., Liu, Q.H., Song, L.P.: Three-dimensional reconstruction of objects buried in layered media using Born and distorted Born iterative methods. Geosci. Rem. Sens. Lett. IEEE 1(2), 107–111 (2004). https://doi.org/10.1109/lgrs.2004.826562
40. Wei, Z., Chen, X.: Deep-learning schemes for full-wave nonlinear inverse scattering problems. IEEE Trans. Geosci. Rem. Sens. 57(4), 1849–1860 (2019). https://doi.org/10.1109/tgrs.2018.2869221
41. Puzyrev, V.: Deep learning electromagnetic inversion with convolutional neural networks. Geophys. J. Int. 218(2), 817–832 (2019). https://doi.org/10.1093/gji/ggz204
42. LeCun, Y., Cortes, C.: MNIST Handwritten Digit Database. (2010)
43. Hughes, T.W., et al.: Forward-mode differentiation of Maxwell's equations. ACS Photonics 6(11), 3010–3016 (2019). https://doi.org/10.1021/acsphotonics.9b01238
44. Pearson, K.: LIII. On lines and planes of closest fit to systems of points in space. London, Edinburgh Dublin Phil. Mag. J. Sci. 2(11), 559–572 (1901). https://doi.org/10.1080/14786440109462720
45. Gisbrecht, A., Schulz, A., Hammer, B.: Parametric nonlinear dimensionality reduction using kernel t-SNE. Neurocomputing 147, 71–82 (2015). Advances in Self-Organizing Maps Subtitle of the special issue: Selected Papers from the Workshop on Self-Organizing Maps 2012 (WSOM 2012). Available from: https://doi.org/10.1016/j.neucom.2013.11.045
46. Van der Maaten, L., Hinton, G.: Visualizing data using t-SNE. J. Mach. Learn. Res. 9(11) (2008)
47. Pedregosa, F., et al.: Scikit-learn: machine learning in Python. J. Mach. Learn. Res. 12, 2825–2830 (2011)
48. xgboost developers: XGBoost, An Optimized Distributed Gradient Boosting Library. https://xgboost.readthedocs.io/ (2022)
49. Chen, T., Guestrin, C.: XGBoost: a scalable tree boosting system. In: Proceedings of the 22nd ACM SIGKDD International Conference on Knowledge Discovery and Data Mining, pp. 785–794. ACM, New York (2016). KDD '16
50. Bergstra, J., Bengio, Y.: Random search for hyper-parameter optimization. J. Mach. Learn. Res. 13(2) (2012)
51. Chollet, F., et al. Keras (2015). https://keras.io
52. Martin, A., et al.: TensorFlow: Large-Scale Machine Learning on Heterogeneous Systems (2015). Software available from tensorflow.org. https://www.tensorflow.org/
53. He, K., et al.: Delving deep into rectifiers: surpassing human-level performance on ImageNet classification. In: 2015 IEEE International Conference on Computer Vision (ICCV), pp. 1026–1034 (2015)
54. Rumelhart, D.E., McClelland, J.L.: Learning Internal Representations by Error Propagation, pp. 318–362 (1987)

55. Brown, P., et al.: A statistical approach to language translation. In: Coling Budapest 1988 Volume 1: International Conference on Computational Linguistics (1988)
56. Kingma, D.P., Ba, J.: Adam: A Method for Stochastic Optimization. (2014)
57. Tsoumakas, G., Katakis, I.: Multi-label classification: an overview. Int. J. Data Warehous. Min. 3(3), 1–13 (2007). https://doi.org/10.4018/jdwm.2007070101
58. Kaczmarek, M., Buchnev, O., Nandhakumar, I.: Ferroelectric nanoparticles in low refractive index liquid crystals for strong electro-optic response. Appl. Phys. Lett. 92(10), 103307 (2008). https://doi.org/10.1063/1.2884186

How to cite this article: Simsek, E., Manyam, H.R.: Classification with electromagnetic waves. IET Microw. Antennas Propag. 1–13 (2024). https://doi.org/10.1049/mia2.12522